# Parameter optimization for the latest quark-meson coupling energy-density functional

K. L. Martinez and A. W. Thomas ⓞ
*CSSM and CoEPP, Department of Physics, University of Adelaide, South Australia 5005, Australia*

J. R. Stone
*Department of Physics (Astro), University of Oxford, Oxford OX1 3RH, United Kingdom*
*and Department of Physics and Astronomy, University of Tennessee, Tennessee 37996, USA*

P. A. M. Guichon
*IRFU-CEA, Université Paris-Saclay, F91191 Gif sur Yvette, France*

The quark-meson-coupling (QMC) model self-consistently relates the dynamics of the internal quark structure of a hadron to the relativistic mean fields arising in nuclear matter. It offers a natural explanation to some open questions in nuclear theory, including the origin of many-body nuclear forces and their saturation, the spin-orbit interaction, and properties of hadronic matter at a wide range of densities. The QMC energy density functionals QMC-I and QMCπ-I have been successfully applied to calculate ground state observables of finite nuclei in the Hartree-Fock + BCS approximation, as well as to predict properties of dense nuclear matter and cold nonrotating neutron stars. Here we report the latest development of the model, QMCπ-II, which includes higher order terms in density in the expansion of the relativistic energy-density functional, as well as the self-interaction of the $\sigma$ meson. A derivative-free optimization algorithm has been employed to determine a new set of the model parameters and their statistics, including errors and correlations. QMCπ-II predictions for a wide range of properties of even-even nuclei across the nuclear chart, with fewer adjustable parameters, are comparable with other models. The nuclear incompressibility is significantly reduced in this version, leading to a description of giant monopole resonances which is consistent with experimental data.

## I. INTRODUCTION

The quark-meson-coupling (QMC) model is based on the self-consistent adjustment of the internal structure of hadrons immersed in a nuclear medium in which there are strong Lorentz scalar and vector mean fields [1,2]. These changes lead naturally to the appearance of many-body nuclear forces through higher-order terms in density in the QMC energy-density functional (EDF) [3,4]. The model has been applied to a wide range of problems of experimental interest [5], including the possible existence of meson-nucleus bound states [6,7] and the structure of hypernuclei [8].

The first systematic application of the QMC model in the Hartree-Fock (HF) + BCS framework to a wide range of even-even nuclei (QMC-I) [9] produced promising results with fewer and well constrained free parameters as compared to the traditional and frequently used EDF of the Skyrme type. The accuracy with which the ground state binding energies of superheavy nuclei were reproduced, although they were not included the fitting procedure, was particularly encouraging. This feature was explored further in Ref. [10], using the next development of the model by including one-pion-exchange (QMCπ-I).

In this work, we report the latest version of the QMC model (QMCπ-II), where the earlier version has been extended to include higher order terms in density in the expansion of

the EDF, especially in the finite range and kinetic terms. In addition, it includes the self-interaction of the $\sigma$ meson [11]. Modern search procedures were used to optimize the model parameters to give the best fit to known ground state properties of a large number of magic and semimagic nuclei, while retaining consistency with empirical nuclear matter properties at saturation.

This paper is organized as follows: Section II gives a short outline of the main features of the QMC EDF; the method of obtaining the QMCπ-II parameter set as well the statistics necessary to validate the results against experiment are presented in Sec. III; Sec. IV contains assessment of the quality of the fit and summarizes the main results together with their analysis and discussion, followed by Sec. V with main conclusions and outlook for future study.

## II. THEORETICAL FRAMEWORK

### A. QMCπ-II EDF

The full derivation of the EDF can be found in the recent review [11]. Here we outline only the main features of the model. The basic idea is to apply self-consistently a scalar mean field $\sigma$ to a bound nucleon which has internal structure, responsive to the effect of the external field. While the structure of the intermediate range attraction between two

nucleons is undoubtedly complex, involving various types of two-pion exchange as well as the exchange of the observed $\sigma$ meson, relativistic models have enjoyed considerable success replacing all of this by the exchange of effective mesons ($\sigma, \omega, \rho$). This approach is adopted in the QMC model.

Assuming that the nucleon is modeled as the MIT bag, the equation of motion of the bag in the external fields can be derived. Solution of the equation of motion of a bag in a constant field yields an effective mass which can be approximated as

$$M_B^* = M_B - g_\sigma \sigma + \frac{d}{2}(g_\sigma \sigma)^2, \tag{1}$$

where $g_\sigma \sigma$ is the strength of the scalar field, $g_\sigma$ is the coupling of the scalar meson to the free nucleon and is related to the quark-meson coupling, and $d$ is the scalar polarizability. It quantifies the effects of the scalar field on the nucleon structure and is determined within the model to a good approximation as $d \approx 0.18 R_B$, with $R_B$ being the bag radius. The coupling of the nucleon with the vector meson fields, $g_\omega \omega$ and $g_\rho \rho$, does not affect the internal structure of the bag but contributes a constant shift to its energy.

When applied to finite nuclei, we consider a bag in meson fields which vary slowly as a function of position and assume that in the nucleus the meson fields essentially follow the nuclear density. This assumption should secure the instantaneous adjustment of the motion of the quarks, which are relativistic, to the actual value of the field.

Taking the nuclear system as a collection of nonoverlapping bags, the *classical* total energy can be written as a sum of contributions from the bag motion and the meson fields [11],

$$E_{\text{QMC}} = \sum_{i=1,\dots} \sqrt{P_i^2 + M_i^2(\sigma(\vec{R}_i))} + g_\omega^i \omega(\vec{R}_i)$$
$$+ g_\rho \vec{I}_i \cdot \vec{B}(\vec{R}_i) + E_\sigma + E_{\omega,\rho}, \tag{2}$$

where $\vec{R}_i$ and $\vec{P}_i$ are the position and momentum of a baryon $i$ and $\vec{I}$ is the isospin matrix. Following the notation of Ref. [11], $\vec{B}$ stands here for the isovector $\rho$ field, to avoid confusion with the baryon number density $\rho$ used in Sec. III A.

The energy of the $\sigma$ field is

$$E_\sigma = \int d\vec{r} \left[ \frac{1}{2}(\vec{\nabla}\sigma)^2 + V(\sigma) \right] \tag{3}$$

and the expressions for $E_{\omega,\rho}$ are analogous. The potential energy in (3), $V(\sigma) = m_\sigma^2 \sigma^2/2 + \cdots$, is generally limited to the quadratic term. This was the case in the QMC-I and QMC$\pi$-I models. Here we take a more general form [11],

$$V(\sigma) = \frac{m_\sigma^2 \sigma^2}{2} + \frac{\lambda_3}{3!}(g_\sigma \sigma)^3 + \frac{\lambda_4}{4!}(g_\sigma \sigma)^4. \tag{4}$$

This extension involves an additional parameter $\lambda_3$ which must be obtained from a fit to experimental data. The quartic term is added to guarantee the existence of a ground state. The constant $\lambda_4$ may be arbitrarily small but must be positive. It has been set to zero in the present work because we are not concerned with the limit of large $g_\sigma \sigma$. The generalization allows a contribution of the $\sigma$ exchange in the $t$ channel to the polarizability, that cannot arise from the response of the bag

to the $\sigma$ field. This extension leads to a significant improvement of the QMC$\pi$-II predictions of saturation properties of symmetric nuclear matter.

After quantization, the Hamiltonian $H_{\text{QMC}}$, corresponding to the classical energy (2), still depends on the meson fields. They are eliminated through the equations of motion:

$$\frac{\delta H_{\text{QMC}}}{\delta \sigma(\vec{r})} = \frac{\delta H_{\text{QMC}}}{\delta \omega(\vec{r})} = \frac{\delta H_{\text{QMC}}}{\delta B(\vec{r})} = 0. \tag{5}$$

In practice, we write the meson field operator $\sigma = \bar{\sigma} + \delta\sigma$ (and similarly for the other mesons) where $\bar{\sigma}$ is the expectation value $\langle \sigma \rangle$ determined by the mean field equation

$$\frac{\langle \delta H_{\text{QMC}} \rangle}{\delta \bar{\sigma}} = 0 \tag{6}$$

and the $\delta\sigma$ is a fluctuation determined as a perturbation around the mean field. In our HF approximation, the fluctuations generate the Fock term. The full QMC Hamiltonian reads

$$H_{\text{QMC}} = H_\sigma + H_\omega + H_\rho + H_{so} + H_\pi, \tag{7}$$

with the detailed expressions given in Ref. [11]. Note that for consistency the density dependent modification of the mass of the $\sigma$ meson is not yet included.

The first three terms in Eq. (7) are spin independent. The spin-orbit term, $H_{so}$, arises naturally within the model from the first order correction associated with the variation of the external field over the volume of the nucleon (see for details Sec. 2.2.2 of Ref. [11]). It is fully expressed in terms of the existing QMC parameters. The pion exchange, because of its long range character, is calculated as a perturbation in a local density approximation [11] and does not introduce additional free parameters.

The Hamiltonian (7) is used to develop the QMC EDF in HF calculation of finite nuclei,

$$\mathcal{E}_{\text{QMC}} = \langle \Phi | H_{\text{QMC}} | \Phi \rangle. \tag{8}$$

The expectation value of $\langle H_{\text{QMC}} \rangle$ in a Slater determinant $\Phi$ for $Z$ protons and $N$ neutrons, obtained by filling the single-particle states $\{\phi^i(\vec{r}, \sigma, m)\}$ up to a Fermi level $F_m$ with $m = \pm 1/2$ being the isospin projection such that $p \leftrightarrow 1/2, n \leftrightarrow -1/2$, is calculated as a function of density $\rho$, kinetic energy density $\tau$, and spin-orbit density $\vec{J}$,

$$\rho_m(\vec{r}) = \sum_{i \in F_m} \sum_\sigma |\phi^i(\vec{r}, \sigma, m)|^2, \quad \rho = \rho_p + \rho_n, \tag{9}$$

$$\tau_m(\vec{r}) = \sum_{i \in F_m} \sum_\sigma |\vec{\nabla}\phi^{i*}(\vec{r}, \sigma, m)|^2, \quad \tau = \tau_p + \tau_n, \tag{10}$$

$$\vec{J}_m = i \sum_{i \in F_m} \sum_{\sigma\sigma'} \vec{\sigma}_{\sigma'\sigma} \times [\vec{\nabla}\phi^i(\vec{r}, \sigma, m)]\phi^{i*}(\vec{r}, \sigma', m),$$

$$\vec{J} = \vec{J}_p + \vec{J}_n. \tag{11}$$

### B. Pairing and Coulomb terms

Pairing and Coulomb terms are not included in the QMC model. For modeling of finite nuclei, QMC$\pi$-II EDF is augmented by $\mathcal{E}_{\text{pair}}$, based on the BCS model with $\delta$-function

pairing interaction acting through the whole nuclear volume [12],

$$\mathcal{E}_{\text{pair}} = \frac{1}{4} \sum_{q \in (p,n)} V_q^{\text{pair}} \int d^3 r \chi_q^2, \quad \chi_q(\vec{r}) = \sum_{\alpha \in q} u_\alpha v_\alpha |\phi_\alpha(\vec{r})|^2,$$

(12)

where $q \in (p,n)$, $v_\alpha, u_\alpha = \sqrt{1-v_\alpha^2}$ are the occupation amplitudes and $\alpha$ stands for quantum numbers of a single-particle state. The two pairing strengths $V_p^{\text{pair}}$ and $V_n^{\text{pair}}$ for proton and neutron are two additional parameters to be fitted to experimental data.

The Coulomb term is taken in its standard form [13],

$$\mathcal{E}_{\text{Coulomb}} = e^2 \frac{1}{2} \int d^3 r d^3 r' \frac{\rho_p(\vec{r})\rho_p(\vec{r}')}{|\vec{r}-\vec{r}'|}$$
$$- \frac{3}{4} e^2 \left(\frac{3}{\pi}\right)^{1/3} \int d^3 r [\rho_p]^{4/3}, \quad (13)$$

including the exchange term in the Slater approximation. $\rho_p$ stands for density distribution of pointlike protons.

### III. METHOD

The HF+ BCS calculation was performed using the computer code code SKYAX, allowing for axially symmetric and reflection-asymmetric shapes, adapted by Reinhard [9,14] for use with QMC-type EDF. The minimization process was performed in two ways, either without any additional constraint of the path to the final minimum or applying a constraint (CHF) requiring a fixed value of quadrupole moment $\langle Q_2 \rangle = \frac{3}{4\pi} A R_0^2 \beta_2$ with $A$ being a mass number and $R_0 = 1.2$ fm. The latter procedure, particularly useful for calculation of ground state shapes of axially deformed nuclei in terms of the quadrupole deformation parameter $\beta_2$, involves determination of the equilibrium wave functions and single-particle energies at each chosen value of $\beta_2$ used to calculate the quadrupole moment. Changing the deformation parameter by a fixed amount through an expected range of deformations yields the lowest energy of the system and its equilibrium shape.

The QMC$\pi$-II EDF depends on three effective coupling constants $G_\sigma$, $G_\omega$, and $G_\rho$,

$$G_\sigma = \frac{g_\sigma^2}{m_\sigma^2}, \quad G_\omega = \frac{g_\omega^2}{m_\omega^2}, \quad G_\rho = \frac{g_\rho^2}{m_\rho^2}, \quad (14)$$

the $\sigma$ meson mass $m_\sigma$, and the $\sigma$ self-interaction parameter $\lambda_3$. With the two pairing strengths $V_p^{\text{pair}}$ and $V_n^{\text{pair}}$, there are seven free parameters that need to be fitted to experimental data. The remaining parameters of the model, the $\omega$ and $\rho$ meson masses, and the isoscalar and isovector magnetic moments, which appear in the spin-orbit interaction [11], were taken at their physical values. The MIT bag radius $R_B$ was set to 1 fm.

The fit has been performed first to properties of infinite nuclear matter and further narrowed down using extensive data on ground state observables of even-even finite nuclei.

### A. Nuclear matter properties (NMPs)

The EDF (8) significantly simplifies in infinite nuclear matter, a medium with uniform density $\rho$ without surface

and spin-orbit effects. All gradient terms vanish and $\langle H_{\text{QMC}} \rangle$ reduces to $\langle H_{\text{NM}} \rangle$. The binding energy per particle of cold matter containing protons and neutrons is expressed as a function of density and the proton-neutron ratio,

$$\frac{E}{A}(\rho, I) = \frac{\langle H_{NM} \rangle}{\rho}(\rho, I), \quad (15)$$

where $\rho = \rho_p + \rho_n$ is the total density and $\rho_{p,n}$ are proton and neutron number densities. The neutron excess $I$ is defined as the ratio of the difference between the number of neutrons $N$ and protons $Z$ to the mass number $A$ of the nucleus, $I = (N-Z)/A$.

Symmetric nuclear matter (SNM), with $N$ equal to $Z$ and thus $I = 0$, is bound at the saturation point $\rho_0 \sim 0.16$ fm$^{-3}$ with energy $E_0 \sim -16$ MeV. It is customary to use properties of the SNM at saturation, derived from $E/A$ at $\rho_0$ to constrain parameters of nuclear structure models. In this work we employ the symmetry energy $S_0$, its slope $L_0$, and the incompressibility $K_0$.

The symmetry energy $S_0$ is defined as the difference between $E/A$ of symmetric and pure neutron matter,

$$S_0 = \frac{E}{A}(\rho_0, I=0) - \frac{E}{A}(\rho_0, I=1). \quad (16)$$

$S_0(\rho)$ can be expanded about $E/A$ with the second-order term being related to the *asymmetry coefficient* $a_{\text{sym}}$ in the semiempirical mass formula

$$a_{\text{sym}} = \frac{1}{2} \frac{\partial^2 (E/A)}{\partial I^2}\bigg|_{I=0}. \quad (17)$$

The slope of the symmetry energy, $L_0$, is

$$L_0 = 3\rho_0 \left(\frac{\partial S}{\partial \rho}\right)\bigg|_{\rho=\rho_0}, \quad (18)$$

and the incompressibility is calculated as

$$K_0 = 9\rho_0^2 \frac{\partial^2 (E/A)}{\partial \rho^2}\bigg|_{\rho=\rho_0}. \quad (19)$$

### B. Observables for finite nuclei

The requirement on input data for adjustment of the parameters of the QMC$\pi$-II is, as usual, to be known from experiment with high accuracy and least affected by correlations beyond mean field. The first obvious choice is the ground state binding energy BE which is directly available from solution of the mean field equations and can be readily extracted from highly precise measurements of atomic masses.

The second choice relates to the density distribution of protons in the nucleus. Elastic electron scattering and optical methods provide information on the charge density distribution of a nucleus and, in particular, its mean-square charge radius $\langle R_{\text{ch}}^2 \rangle$. The model calculation provides the mean-square radius of the proton distribution, $\langle R_p^2 \rangle$, assuming the protons are pointlike particles without internal structure. The two quantities are related by [15]

$$\langle R_{ch}^2 \rangle = \langle R_p^2 \rangle + \langle r_p^2 \rangle + \frac{N}{Z} \langle r_n^2 \rangle, \quad (20)$$
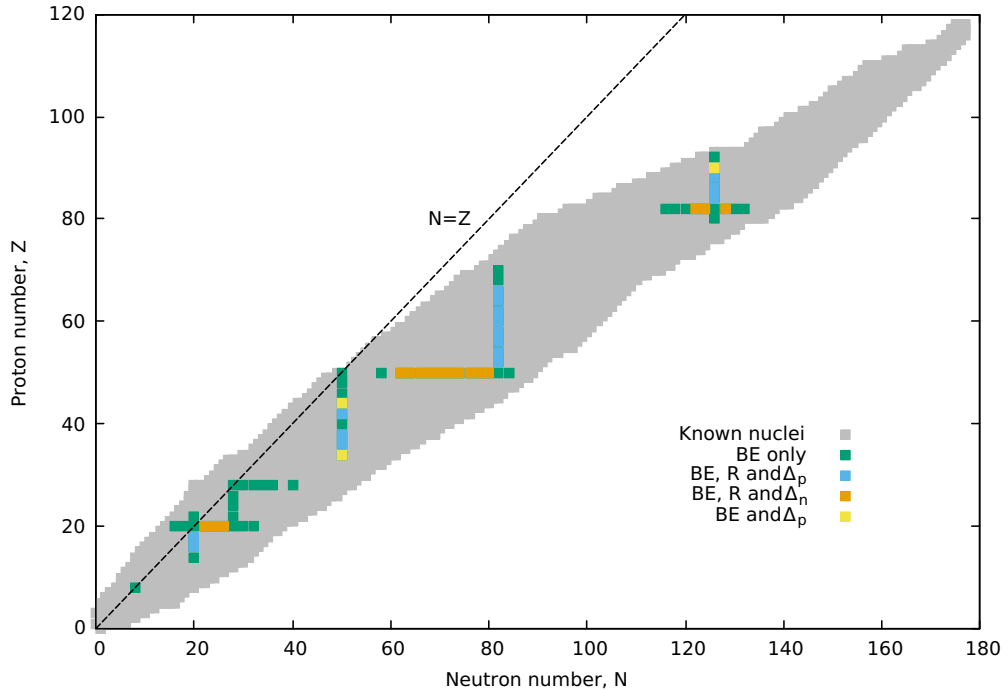
FIG. 1. Doubly magic and semimagic nuclei included in the fit. The nuclear observables and number of data points per nucleus entering the fitting procedure are indicated. For more explanation see the text.

with the free proton and neutron charge radii taken as $\langle r_p^2 \rangle =$ 0.7071 fm$^2$ and $\langle r_n^2 \rangle = -0.1161$ fm$^2$ [16]. Note that the standard relation in Eq. (20) is valid for spherical nuclei. In Ref. [17], additional terms appear in Eq. (20) for charge radii in deformed nuclei.

Finally, because we work in the HF + BCS framework, data are needed to constrain parameters of the pairing EDF (12), added to the QMC EDF. The pairing gap, a measure of nuclear pairing correlations, is a quantity that can be extracted from experimental odd-even staggering in binding energies, e.g., the neutron gap [13],

$$\Delta_n^{(5)} = -\tfrac{1}{8}E(Z, N+2) + \tfrac{1}{2}E(Z, N+1) - \tfrac{3}{4}E(Z, N)$$
$$+ \tfrac{1}{2}E(Z, N-1) - \tfrac{1}{8}E(Z, N-2), \qquad (21)$$

and an equivalent expression for the proton gap. However, it is complicated to calculate the gaps in mean field models [13,18], in particular in a model including only even-even nuclei, and is not applicable if some of the nuclei are deformed.

We therefore adopt as a measure of pairing correlations the average spectral gap (for details see Ref. [18]),

$$\bar{\Delta}_q = \frac{\sum_{\alpha \in q} u_\alpha v_\alpha \Delta_\alpha}{\sum_{\alpha \in q} u_\alpha v_\alpha}, \qquad (22)$$

where $v_\alpha$, $u_\alpha = \sqrt{1 - v_\alpha^2}$ are the occupation amplitudes and $\Delta_\alpha$ is the state-dependent single-particle pairing gap [19].

As noted in [13], $\bar{\Delta}_q$ and $\Delta_{n,p}^{(5)}$ are reasonably well related in midshell regions but exhibit different behavior in the vicinity of (semi)magic nuclei which may introduce a larger difference between experiment and model predictions.

### C. Parameter constraints

The bounds for the QMC$\pi$-II parameters were determined by first establishing the range of values over which combinations of the model parameters reproduce the properties of nuclear matter within reasonable bounds. For symmetric nuclear matter, $\rho_0$ and $E_0$ are widely accepted to be 0.16 fm$^{-3}$ and $-16$ MeV, respectively. Here, the search range was allowed to be within 10% of the accepted values. Reference [20] summarizes 28 available results from various terrestrial measurements and astrophysical observations for $a_{\text{sym}}$ which varies from around 29 to 33 MeV. For the incompressibility, recommended values vary widely over the range 200–315 MeV [21–24]. As we show below, the application of the QMC$\pi$-II model to giant monopole resonances (GMRs) favors the lower end of this range. For the internal consistency of the present model it is important that the $\sigma$ self-interaction parameter $\lambda_3$ not be too large—a large $\lambda_3$ gives a lower incompressibility. This consideration leads us to search for $\lambda_3$ within the range 0.0–0.05. The search for a best fit to the properties of finite nuclei was then carried out within the boundaries defined by these constraints on nuclear matter properties.

Binding energies BE, root-mean-square rms charge radii $R_{\text{ch}}$, and proton and neutron pairing gaps $\Delta_{p,n}$ [calculated using Eq. (22)] for seventy magic and doubly magic nuclei with $Z = 8, 20, 28, 50, 82$ and $N = 126$ were included in the fit. This same set of even-even nuclei was used by Klupfel *et al.* [13] to fit parameters for the Skyrme EDF with the exceptions of some updated values taken for binding energies [25] and for rms charge radii [26]. Figure 1 shows the distribution of the data across the nuclear chart, consisting

of a total of 161 data points. The best parameter set for the fitting to finite nuclei was sought using POUNDerS which is discussed in the next subsection.

### D. Parameter optimization

The search algorithm POUNDerS, which stands for parameter optimization using no derivatives for sums of squares [15], was used for the fitting procedure. POUNDerS is a part of the Toolkit for Advanced Optimization which is made available by the Portable, Extensible Toolkit for Scientific Computation (PETSc) [27–29]. The algorithm has proven to be efficient in optimizing nuclear energy-density functionals of the Skyrme type [15,30,31]. The main advantage of POUNDerS over other optimization procedures is that it employs a derivative-free algorithm, which is highly efficient in terms of the speed, accuracy, and reliability of results [32]. Starting from initial values of the parameters, the total sum of squares of the deviations from experiment, or the chi-squared value ($\chi^2$), is minimized. In this work, the objective function $F(\hat{\mathbf{x}})$ for minimization was chosen to be dimensionless,

$$F(\hat{\mathbf{x}}) = \sum_{i}^{n} \sum_{j}^{o} \left( \frac{\bar{s}_{ij} - s_{ij}}{w_j} \right)^2, \qquad (23)$$

where $n$ is the total number of nuclei, $o$ is the total number of observables, and $s_{ij}$ and $\bar{s}_{ij}$ are the experimental and fitted values, respectively, for each nucleus $i$, and each observable $j$. $w_j$ stands for the *effective* error for each observable, set in this fit to be $w_{BE} = 1$ MeV, $w_{R_{ch}} = 0.02$ fm and $w_{\Delta_{p,n}} = 0.12$ MeV for all nuclei without weighting. These errors, much higher than the errors reported by the experimenters, take into account a realistic estimate of accuracy of the model as well of the fitting procedure.

Following Kortelainen *et al.* [15], the covariance matrix was approximated as

$$\mathrm{Cov}(\hat{\mathbf{x}}) \approx \frac{\chi^2}{d-p}(\mathbf{J^T J})^{-1}, \qquad (24)$$

where $J$ is the Jacobian matrix with derivatives computed using finite differences, $d$ is the total number of data points, and $p$ is the number of parameters. The objective function was evaluated at $\{\hat{\mathbf{x}} \pm \eta e_j\}$, with $\eta$ set to $10^{-3}$ and $e_j$ being the scale used for each parameter during the search.

The square root of the diagonal terms of the covariance matrix gives the *standard deviation* $\sigma$ for each parameter and the off-diagonal terms give the correlation coefficient between any two parameters $x_k$ and $x_l$,

$$\mathrm{Cor}(x_k, x_l) = \frac{\mathrm{Cov}(x_k, x_l)}{\sqrt{\sigma_{x_k}^2 \sigma_{x_l}^2}}. \qquad (25)$$

A *residual* is defined as the difference between the theoretical and experimental results, $\bar{s}_{ij} - s_{ij}$, and is used to evaluate the *root-mean-square deviation* (RMSD) for each observable,

$$\mathrm{RMSD}(j) = \sqrt{\frac{1}{n} \sum_{i}^{n} (\bar{s}_{ij} - s_{ij})^2}. \qquad (26)$$

The *percentage deviation* from experiment is $100 \times (\frac{\bar{s}_{ij} - s_{ij}}{\bar{s}_{ij}})$.

TABLE I. Confidence intervals (CIs) and standard deviation $\sigma$ of the final QMC$\pi$-II parameter set. The proton and neutron pairing strengths are included for completeness.

| Parameter | Value | 95% CI | $\sigma$ |
|---|---|---|---|
| $G_\sigma$ (fm$^2$) | 9.66 | [9.62, 9.70] | 0.02 |
| $G_\omega$ (fm$^2$) | 5.23 | [5.22, 5.24] | 0.01 |
| $G_\rho$ (fm$^2$) | 4.75 | [4.68, 4.83] | 0.04 |
| $m_\sigma$ (MeV) | 494 | [491, 497] | 2 |
| $\lambda_3$ (fm$^{-1}$) | 0.051 | [0.050, 0.052] | 0.001 |
| $V_p^{\mathrm{pair}}$ (MeV) | 258 | [249, 267] | 5 |
| $V_n^{\mathrm{pair}}$ (MeV) | 237 | [228, 246] | 5 |

## IV. RESULTS AND DISCUSSION

In this section the results of the optimization are presented. The final parameter set has been used to calculate ground state observables for the 70 nuclei included in the fit (Sec. IV B) and further applied to calculate binding energies and charge radii for even-even nuclei with experimentally known masses and with $Z \geqslant 8$ (Sec. IV C). Predictions of the model for other observables not included in the fit are discussed (Sec. IV D), along with calculations of ground state binding energies of superheavy even-even nuclei (Sec. IV E).

### A. Parameters

Table I summarizes the best fit QMC$\pi$-II parameter set with their confidence intervals and standard deviations. The NMPs corresponding to this set are $\rho_0 = 0.15 \pm 0.01$ fm$^{-2}$, $E_0 = -15.69 \pm 0.2$ MeV, $a_{\mathrm{sym}} = 28.8 \pm 0.6$ MeV, and $K_0 = 230 \pm 1$ MeV. One important feature of QMC$\pi$-II is the smaller value for the incompressibility of around 230 MeV, which tended to be somewhat high in the previous models, QMC-I [9] and QMC$\pi$-I [11], where the values were 340 and 319 MeV, respectively. The addition of the $\sigma$ self-interaction in the potential energy enhances the saturation effects in the density dependent terms of the QMC model by increasing the effective scalar polarizability, $d \rightarrow \tilde{d} = d + \lambda_3 G_\sigma / 2$. Further in the present model, taking $\sigma$ mass to be density independent and only allowing it to vary during the fitting process corrects the overestimation in the fluctuation part of $H_\sigma$ which was responsible for giving high incompressibility values in previous versions.

Another significant result is that the slope of the symmetry energy $L_0$, not included in the fit but calculated afterwards with the final parameter set, is now $L_0 = 40 \pm 2$ MeV. This is improved compared to the lower values obtained in the previous models QMC-I [9] and QMC$\pi$-I [10,11] which gave $L_0 = 23 \pm 4$ MeV and $L_0 = 17 \pm 1$ MeV, respectively. From Ref. [20], the average values for the symmetry energy and its slope are 31.6 and 58.9 MeV, respectively. The finite-range droplet model combined with folded Yukawa microscopic part (FRDM) [33], for example, has values $a_{\mathrm{sym}} = 32.5 \pm 0.5$ MeV and $L_0 = 70 \pm 15$ MeV. Recently, by studying the radioactivity of 19 proton emitters having large isospin asymmetry, $L_0$ is constrained to have a value of $51.8 \pm 7.2$ MeV [34].

TABLE II. Correlation between QMC$\pi$-II parameters computed as discussed in Sec. III D.

| | $G_\sigma$ | $G_\omega$ | $G_\rho$ | $m_\sigma$ | $V_p^{\text{pair}}$ | $V_n^{\text{pair}}$ | $\lambda_3$ |
|---|---|---|---|---|---|---|---|
| $G_\sigma$ | 1.00 | | | | | | |
| $G_\omega$ | 0.68 | 1.00 | | | | | |
| $G_\rho$ | −0.49 | 0.17 | 1.00 | | | | |
| $m_\sigma$ | 0.38 | −0.24 | −0.83 | 1.00 | | | |
| $V_p^{\text{pair}}$ | 0.19 | 0.05 | −0.26 | 0.16 | 1.00 | | |
| $V_n^{\text{pair}}$ | 0.14 | 0.05 | −0.18 | 0.13 | 0.14 | 1.00 | |
| $\lambda_3$ | −0.07 | 0.33 | 0.82 | −0.78 | −0.19 | −0.14 | 1.00 |

Obviously, all QMC EDFs have correlated parameters and they vary accordingly in the optimization procedure. For the QMC$\pi$-II final parameter set, these correlations are computed as discussed in Sec. III D. Table II shows the correlation between any two parameters of the EDF. A positive (negative) correlation means that parameters are directly (inversely) proportional to each other and a value of 1.0 corresponds to 100% correlation.

Strong positive correlation is seen between the effective couplings $G_\sigma$ and $G_\omega$ as well as between $G_\rho$ and the self-coupling $\lambda_3$ parameter. On the other hand, the $\sigma$ meson mass is inversely dependent on both $G_\rho$ and $\lambda_3$. The introduction of the new $\lambda_3$ parameter in the QMC$\pi$-II model led to a decrease in the three coupling parameters and the value of $m_\sigma$ compared to the QMC-I parameters [9], while it effectively tuned down the incompressibility, $K_0$. For the parameters of the pairing EDF, both proton and neutron pairing strengths have less than 20% positive correlation to $G_\sigma$ and $m_\sigma$ and a very small correlation to $G_\omega$. Furthermore, both pairing parameters are inversely proportional to $G_\rho$ and $\lambda_3$ but with the highest correlation just 26%. This means that changes in the coupling parameters and thus NMP values do not significantly affect the pairing strengths.

### B. Nuclei included in the fit

Table III shows a summary of *percent* deviations of the observables for the 70 finite nuclei included in the fit in comparison with the previous QMC-I [9] and QMC$\pi$-I [10,11] and results from Skyrme force SV-min [13]. It should be noted that QMC-I, QMC$\pi$-I, and SV-min fits included data on diffraction radii and surface thickness which were not included in the current fit for QMC$\pi$-II.

TABLE III. Percentage deviations of observable properties of the nuclei included in the QMC$\pi$-II fit. QMC-I [9] and QMC$\pi$-I [10,11] are results from previous versions of the QMC model. The results from the Skyrme force SV-min [13] are added for comparison.

| Data | QMC$\pi$-II | QMC$\pi$-I | QMC-I | SV-min |
|---|---|---|---|---|
| Binding energy | 0.48 | 0.46 | 0.36 | 0.24 |
| rms charge radius | 0.59 | 0.48 | 0.71 | 0.52 |
| Proton pairing gap | 10.7 | 15.3 | 25.3 | 15.5 |
| Neutron pairing gap | 21.4 | 24.0 | 57.6 | 17.6 |

The QMC$\pi$-II model, with inclusion of the $\sigma$ self-interaction together with the current fitting procedure, showed slight changes in the predictions for finite nuclei observables compared to the previous QMC versions. The deviation for charge radii is higher compared to that of QMC$\pi$-I but pairing gaps are somewhat improved. It must be noted that while the quality of fit for finite nuclei remains comparable in the current model, the nuclear matter properties, specifically $K_0$ and $L_0$, are greatly improved.

Figure 2 illustrates the *percent* deviation from experiment for BE and $R_{\text{ch}}$ of the 70 nuclei, including $Z = 20$, 28, 50, and 82 isotopes and $N = 20$, 28, 50, 82, and 126 isotones. It can be seen that the QMC$\pi$-II results follow almost the same trends as the other models, having relatively higher deviations for lighter nuclei $Z$, $N < 28$ for BE and $R_{\text{ch}}$. Both the BE and rms charge radii *absolute* deviations are up to 2%. For the fit to pairing gaps, deviations are typically within 20% for $\Delta_p$ and up to 40% for $\Delta_n$ with relatively high values for tin isotopes in the midshell region.

### C. Extended results of binding energies and charge radii across the nuclear chart.

Figure 3 illustrates the performance of QMC$\pi$-II for a set of 739 even-even nuclei with known masses, of which 342 have known rms charge radii. This set includes the 70 nuclei included in the QMC$\pi$-II fit which was discussed in Sec. IV B. The binding energy residuals vary within around $\pm 8$ MeV and the charge radius residuals are within $\pm 0.1$ fm. These are essentially the same ranges found for SV-min, DD-ME$\delta$, and UNEDF1 but with a different distribution of residual values across the nuclear chart. The QMC$\pi$-II RMSD for all nuclei included in the plot is 2.34 MeV for masses and 0.03 fm for radii.

The current QMC$\pi$-II parameter set predicts overbinding in most of the nuclei with $N = Z$ and the residuals are relatively higher for these nuclei compared with the other models. $N = Z$ nuclei are known to exhibit the Wigner effect [36] that must be accounted for in the binding energy. Furthermore, the QMC$\pi$-II parameter set predicts mostly underbinding on the neutron-rich side, as shown in Fig. 3. There are also relatively larger errors around the magic isotones $N = 50$ and 82 and in the uranium region.

For charge radii in Fig. 3, note that they have been calculated using the standard relation in Eq. (20). QMC$\pi$-II residuals for $R_{\text{ch}}$ are relatively higher near the $Z = 82$ shell closure, specifically in the mercury ($Z = 80$) region. Neutron-deficient lead isotopes are mostly spherical from laser spectroscopy experiments but mercury and platinum ($Z = 78$) isotopes with neutron number around $N = 104$ show deformations when compared with droplet model calculations [37,38].

To compare the performance of QMC$\pi$-II with other models, binding energy and rms charge radii residuals were also computed for exactly the same set of nuclei included in Fig. 3. Table IV presents the RMSD computed using Eq. (26). Overall, QMC$\pi$-II results appear to be more or less on par with other models. FRDM gives the best predictions for masses with an RMSD of 0.68 MeV but there is no available record of its predictions for charge radii.
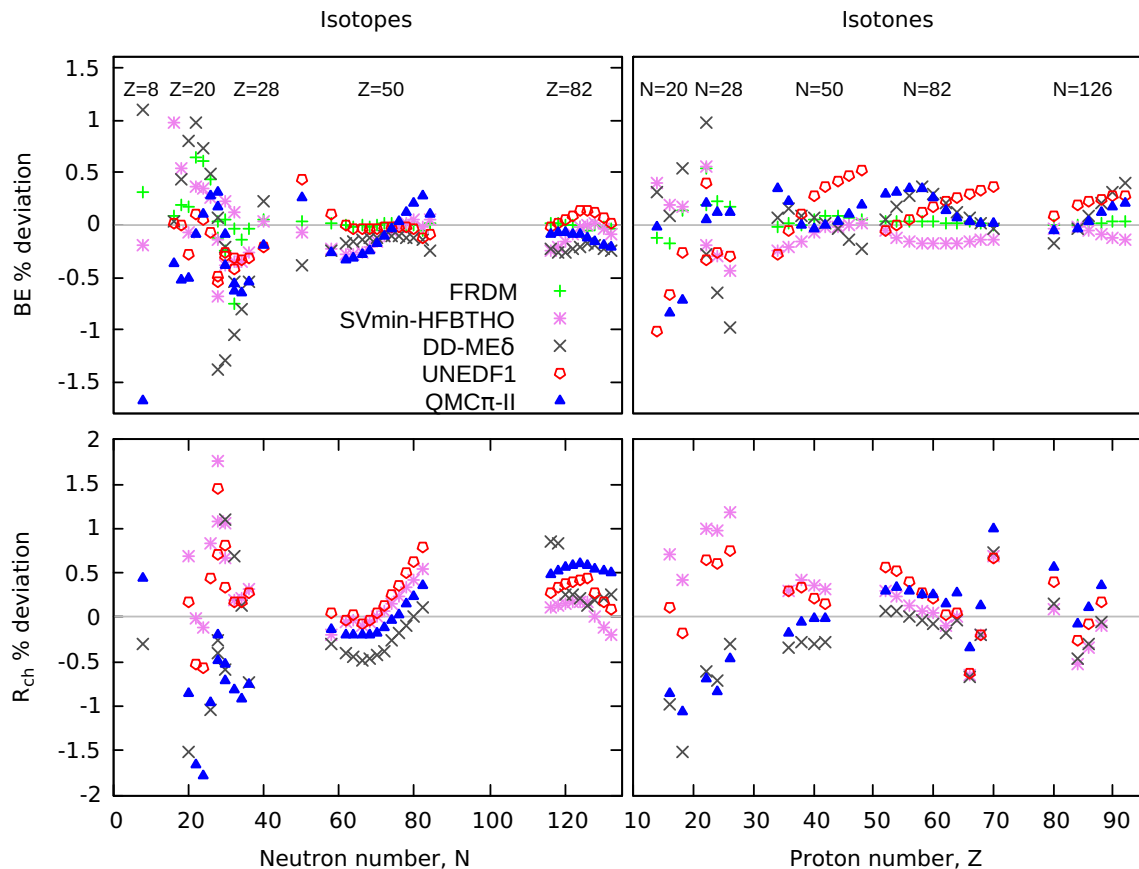
FIG. 2. Percentage deviation from experiment for binding energies BE, rms charge radii $R_{ch}$, and pairing gaps $\Delta_{p,n}$ for the 70 nuclei included in the fit. Added for comparison are the Skyrme type force SV-min [13] and UNEDF1 [30], a covariant energy density DD-ME$\delta$ [35], and the finite-range droplet model (FRDM) [33]. The plot legend is located in the top left panel.

### D. Observables not included in the fit

#### 1. Two-nucleon separation energies

Separation energies provide important information about shell closures and the existence and location of drip lines. Two-nucleon separation energy is defined as the amount of energy needed to remove two nucleons from a particular nucleus. Figure 4 shows the residuals for even-even nuclei with available data for two-proton ($S_{2p}$) and two-neutron ($S_{2n}$) separation energies, comparing results from QMC$\pi$-II and SV-min. Both models are within the same range of residuals.

In particular, two-neutron separation energies for the magic isotopes calcium, nickel, tin, and lead are shown in Figs. 5 and 6. Shell closures at $N = 28$ for the Ca and Ni isotopes and $N = 50$ for Ni are visible through the sudden dip in the separation energies. The same is true for shell closures at $N = 82$ and $N = 126$ for the Sn and Pb isotopes, respectively.

Compared to other models in Fig. 5, QMC$\pi$-II shows pronounced shell closure at $N = 28$ for both calcium and nickel and at $N = 50$ for nickel. The deviation from experiment is, however, relatively larger at $N < 28$ for calcium as well as around $N = 50$. The expected closure at $N = 20$ for Ca is not as pronounced for QMC$\pi$-II as is the case for SV-min. This is due to a low energy gap in the single-particle spectra of neutrons which is further discussed in Sec. IV D 4. Around the

$N = 126$ closure, the QMC$\pi$-II results are in good agreement with experiment, as shown in Fig. 6.

#### 2. Isotopic shifts in charge radii

In an isotopic chain, the evolution of charge radii with mass number is characterized by the difference between the mean-square charge radii of two isotopes of an element calculated using $\delta \langle r^2 \rangle^{A',A} = \langle r^2 \rangle^{A'} - \langle r^2 \rangle^A$. Here $\langle r^2 \rangle$ is the mean-square charge radius for the isotope with nucleon number $A'$ and $A$ is the reference isotope. Figure 7 shows the shifts in radii for calcium and lead from their stable reference isotope $^{40}$Ca and $^{208}$Pb, respectively. Experimental data are taken from Ref. [26] with updates for Ca isotopes from Refs. [40] and [41].

The QMC$\pi$-II radius computations for both the Ca and Pb isotopes are done under the constraint that they should be spherical. For Ca isotopes, none of the models included in the plot reproduce the trend of the experimental data, where the radius shift initially increases from the reference isotope $^{40}$Ca and then drops to almost zero at $^{48}$Ca. All models predicted a continued increase in the radius shift, starting from $^{40}$Ca. It was reported that this trend can be replicated by the Fayans EDF or with a Skyrme force augmented with Fayans pairing and the inclusion of shifts and odd-even staggering of energy
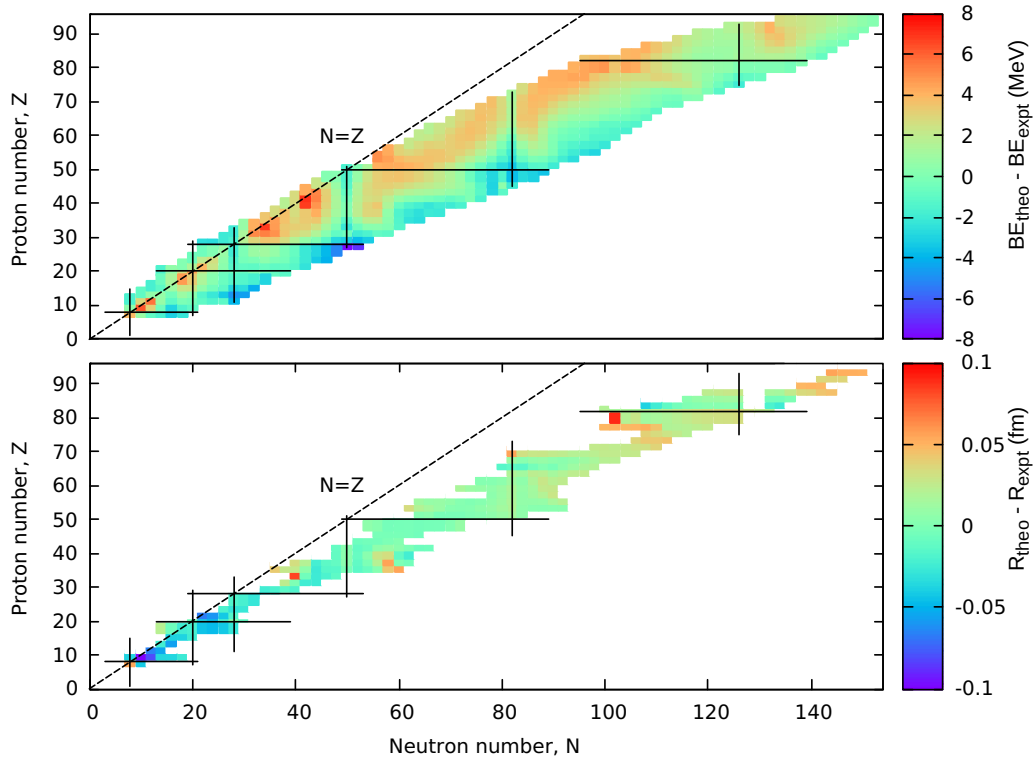
FIG. 3. Binding energy and rms charge radii residuals for 739 even-even nuclei with $Z < 96$. Atomic mass data used to compute the binding energy residuals are taken from Ref. [25] and rms charge radii data are from Ref. [26]. Nuclei with magic numbers are indicated by solid lines.

and radii in the fitting procedure [42]. Taking $^{48}$Ca as the stable reference isotope for isotopic shift to $^{52}$Ca, QMC$\pi$-II predicts a radius shift of 0.294 fm$^2$ and SV-min gives 0.262 fm$^2$, while the recent data yield 0.530(5) fm$^2$ [40]. Certainly this behavior will be studied further as the QMC model continues to develop. Data for $^{36}$Ca and $^{38}$Ca were recently measured and were found to be smaller than $^{40}$Ca but most of the models predicted slightly larger sizes. QMC prediction overestimates the experimental data but predicts that the sizes for the two proton-rich calcium isotopes are smaller than $^{40}$Ca.

For lead isotopes, QMC$\pi$-II and SV-min show almost the same behavior for radius shifts in the neutron-deficient region where experimental data are underestimated, while UNEDF1 predicts oblate deformation for Pb isotopes around $A = 190$. The latter is caused by its low proton state gap at $Z = 82$ [30]. Radius shifts from DD-ME$\delta$ are also higher than those found experimentally for isotopes with $A < 200$. The kink at the doubly magic $^{208}$Pb is not reproduced well by QMC and

TABLE IV. RMSD for binding energies and rms charge radii for QMC$\pi$-II in comparison with Skyrme forces SV-min [13], UN-EDF1 [30], covariant EDF with the DD-ME$\delta$ interaction [35,39], and macroscopic-microscopic FRDM [33].

| Data | QMC$\pi$-II | SV-min | UNEDF1 | DD-ME$\delta$ | FRDM |
|---|---|---|---|---|---|
| Binding energy (MeV) | 2.34 | 3.10 | 2.12 | 2.40 | 0.68 |
| rms charge radius (fm) | 0.03 | 0.02 | 0.03 | 0.03 | |

Skyrme forces and on the neutron-rich side shifts are slightly lower than those found empirically. The isotopic shift from $^{208}$Pb to $^{214}$Pb was considered in Ref. [13], with different values for the effective mass. For QMC$\pi$-II, this Pb radius shift has a value of 0.489 fm$^2$, where the measured value is $0.615 \pm 0.001$ fm$^2$.

### 3. Neutron skin thickness

Another observable relating to size, which is of considerable interest, is the neutron skin thickness $\Delta r_{np}$, defined as the difference between the neutron and proton point radii. Neutron skin thickness has been found to be linearly related to the slope of the symmetry energy for nuclear matter, $L_0$ [43]. Recently, the skin thickness for $^{208}$Pb has been experimentally determined to be $0.15 \pm 0.03$ fm through coherent pion photoproduction [44]. The same value but with an error of $\pm 0.02$ fm has been obtained from antiprotonic x rays while hadron scattering experiments give an average value of $0.17 \pm 0.02$ fm [45]. Figure 8 shows predictions for the skin thickness of those nuclei included in the fit with available experimental values. $\Delta r_{np}$ is plotted against the relative neutron excess, $I = (N - Z)/A$, as defined in Sec. III A. Higher values of $I$ correspond to neutron-rich nuclei, while symmetric nuclei have $I = 0$. In the figure, the gray band is taken from a linear fit of skin thickness experimental data as a function of $I$: $\Delta r_{np}(I) = (-0.03 \pm 0.02) + (0.90 \pm 0.15)I$ [45]

On the proton-rich side ($I < 0$), the mean field models predict a negative value for the skin thickness for $^{36}$Ca and $^{38}$Ca with QMC$\pi$-II values a little lower than the other
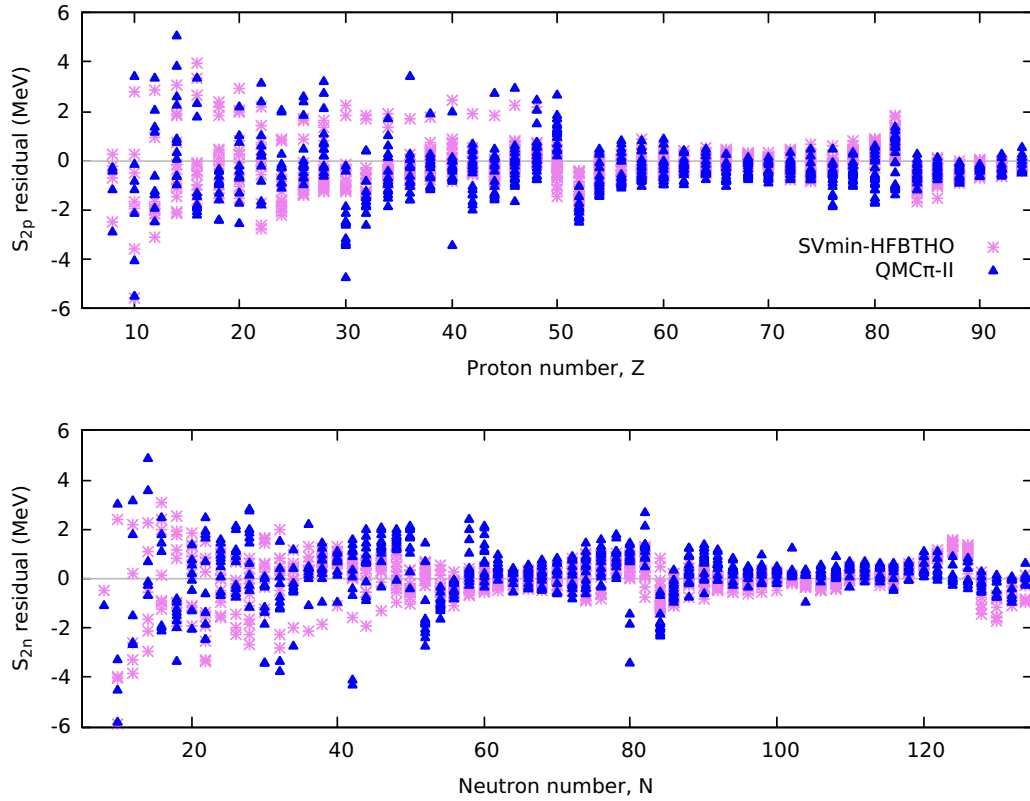
FIG. 4.  Two-nucleon separation energy residual for even-even isotopes and isotones for QMC$\pi$-II and SV-min. Experimental data used to compute the residuals are taken from Ref. [25]. The plot legend is located in the top panel.
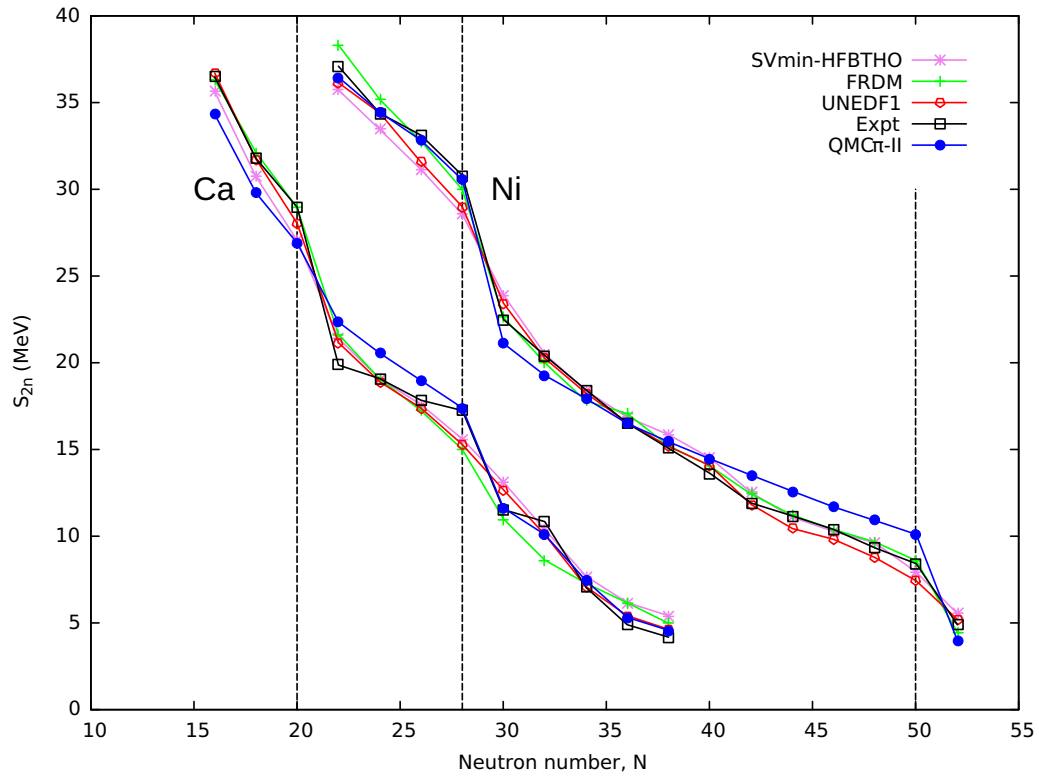


FIG. 5.  Two-neutron separation energies for calcium ($Z = 20$) and nickel ($Z = 28$) isotopes as a function of the neutron number. Shell closures are visible at $N = 28$ for both Ca and Ni and $N = 50$ for Ni isotopes and are indicated by dashed lines. Also added for comparison are results for FRDM [33], SV-min [13], and UNEDF1 [30], taken from Ref. [39] and experimental data from [25].
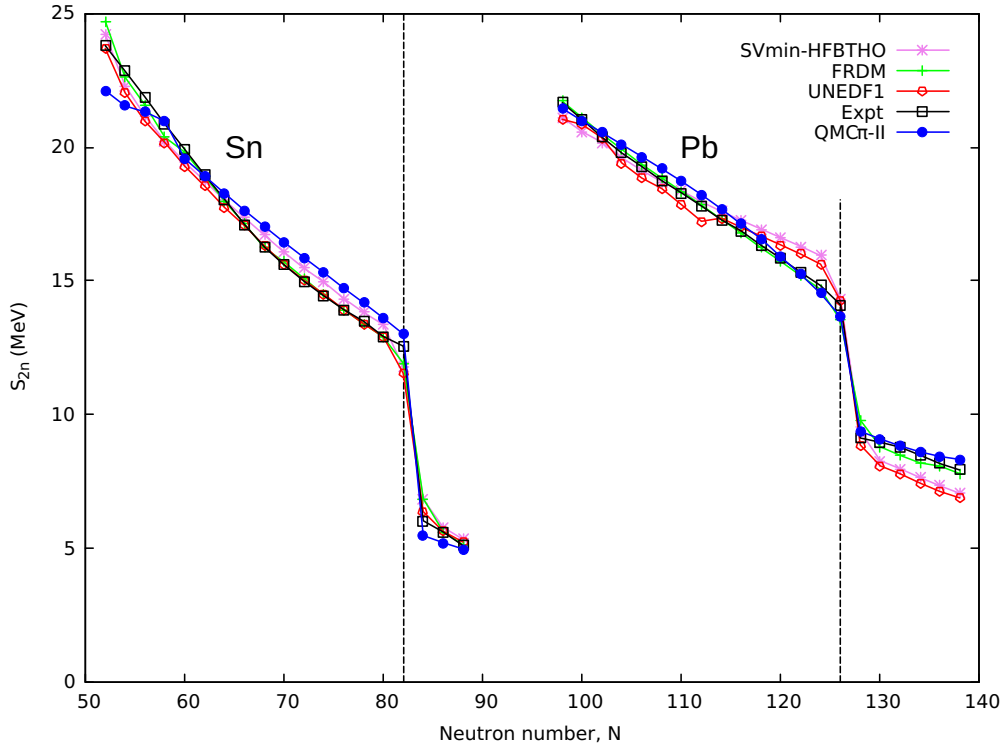
FIG. 6. Same as in Fig. 5 but for tin ($Z = 50$) and lead ($Z = 82$) isotopes. Shell closures are visible at $N = 82$ for Sn and $N = 126$ for Pb isotopes and are indicated by dashed lines.
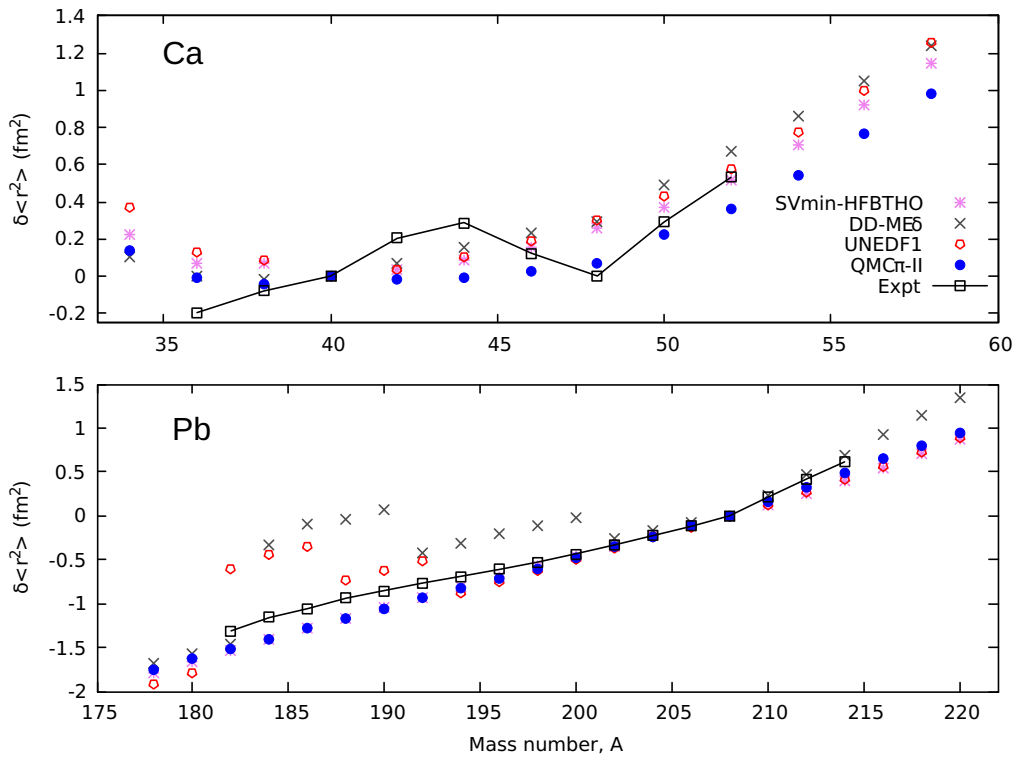


FIG. 7. Isotopic shifts for calcium and lead isotopes with stable reference isotopes $^{40}$Ca and $^{208}$Pb, respectively, plotted against mass number $A$. Added for comparison are values for SV-min [13], DD-ME$\delta$ [35], and UNEDF1 [30], all taken from Ref. [39]. Experimental data are from [26,40,41] and errors are smaller than the symbols used in the plot. Plot legend is located in the top panel.
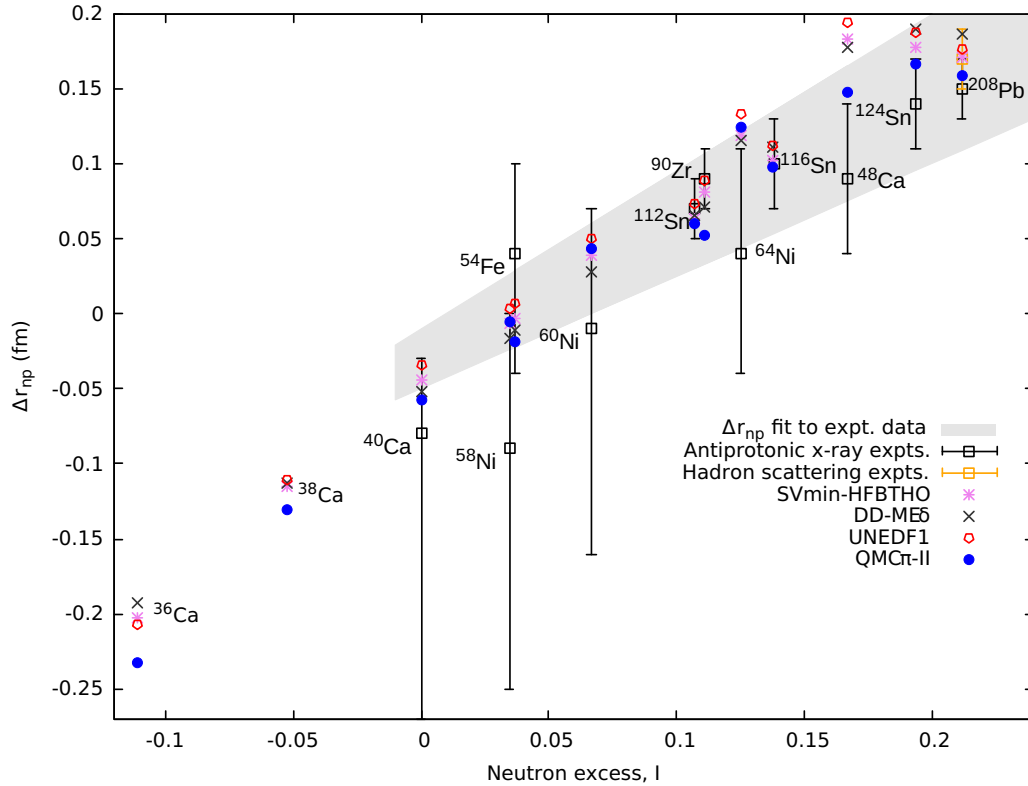
FIG. 8. Skin thickness for nuclei included in the QMC$\pi$-II fit as a function of the neutron excess $I = (N - Z)/A$. Added for comparison are SV-min [13] and DD-ME$\delta$ [35] both taken from Ref. [39] and experimental data from Ref. [45].

models. As with other models, the skin thickness for $^{48}$Ca and $^{64}$Ni are overestimated and are above experimental errors. Towards the neutron-rich side, most values from QMC$\pi$-II are within the error bounds of experiment. The prediction for $^{208}$Pb is in good agreement with data from antiprotonic x rays and is within the error of data deduced from hadron scattering experiments.

### 4. Single-particle states

Figures 9–11 show neutron and proton single states for doubly magic symmetric $^{40}$Ca nuclei as well as for neutron-rich $^{78}$Ni and $^{132}$Sn nuclei. Results for QMC$\pi$-II and SV-min are compared with experimental data from Ref. [46]. Note that the spin-orbit splittings for some doubly magic nuclei were included in the fitting for SV-min but were left out for the present QMC parameter search.

The calculated values for both QMC$\pi$-II and SV-min for the proton single-particle energies of $^{40}$Ca appear to be
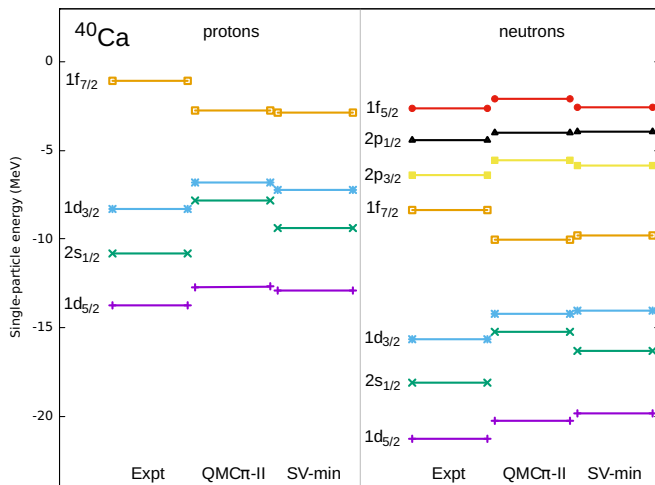


FIG. 9. Proton and neutron single-particle states for $^{40}$Ca. Experimental data are taken from Ref. [46] and SV-min values are from Ref. [39]. Single-particle levels are shown in different colors and labels are placed before the experimental data for each level.
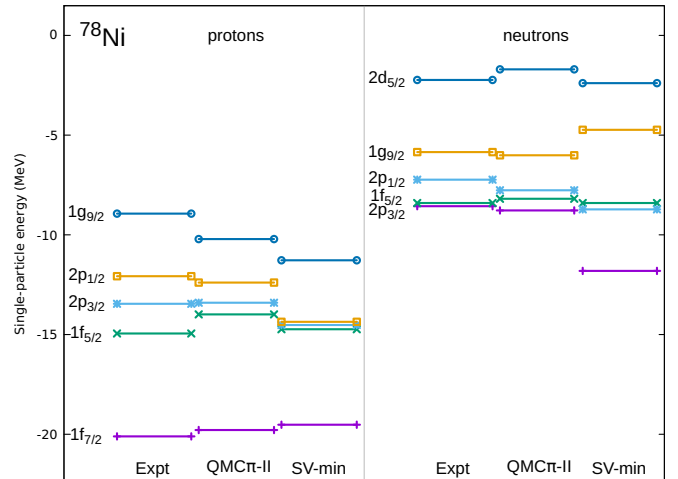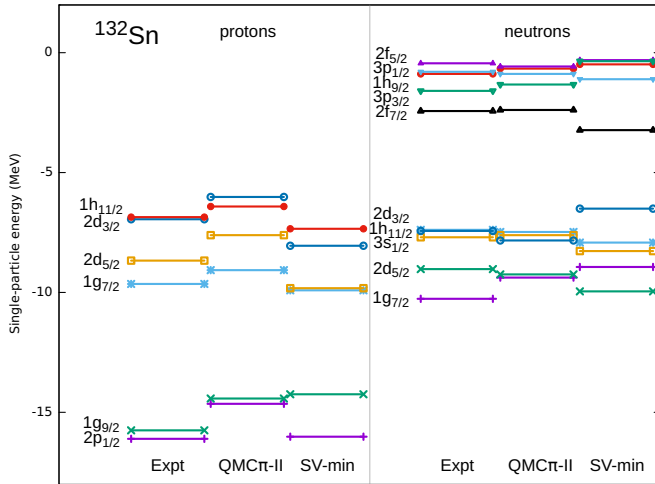


FIG. 10. Same as in Fig. 9 but for $^{78}$Ni.

FIG. 11. Same as in Fig. 9 but for $^{132}$Sn.

squeezed resulting in a low energy gap compared to experiment. This is also true for the case of $^{40}$Ca neutron states which explains the reduction in the shell closure at $N = 20$, as shown in Fig. 5. $^{78}$Ni isotope is not included in the QMC$\pi$-II fit but both proton and neutron states are fairly well reproduced for the QMC model as can be seen in Fig. 10. For $^{132}$Sn, shown in Fig. 11, the proton states are slightly higher compared to data while the neutron states agree reasonably with experiment.

### 5. Nuclear deformations

In Refs. [15,30] several deformed nuclei were included in the fitting for UNEDF0 and UNEDF1 parameter sets. Though our current fitting procedure only includes magic nuclei, which are mostly spherical, the final parameter set can be used to extend the calculations to nuclei having deformations. Figure 12 shows the performance of QMC in comparison with other models and experiment [47] for the deformation parameter $\beta_2$ and transition probability $B(E2)\uparrow$ from the ground state to the first excited $2^+$ state of gadolinium ($Z = 64$) isotopes. As computed in Ref. [47], $B(E2)\uparrow = [(3/4\pi)\beta ZeR_0^2]^2$ where $R_0 = 1.2A^{1/3}$ fm. The intrinsic quadrupole moment $Q_0$ is directly related to the transition probability by the expression $Q_0^2 = (16\pi/5e^2)B(E2)\uparrow$.

The models predict a spherical shape for $^{146}$Gd and prolate shapes for neutron-rich Gd isotopes. We note that the computation here is done in the constrained case and from Fig. 12, isotopes $^{140-144}$Gd are predicted to have oblate shapes as opposed to unconstrained QMC-I results where they were prolate [9]. $B(E2)\uparrow$ values from QMC$\pi$-II agree well with experimental data where available. As with the calculations of radii in Sec. IV C, deformation properties will be the subject of future investigation in the QMC model.

### 6. Giant monopole resonance (GMR)

Isoscalar GMRs are important quantities related to the incompressibility of the symmetric nuclear matter. They are not measured directly but extracted from differential cross sections of inelastic scattering of, typically, $\alpha$ particles but also deuterons at energies of 35–100 MeV per nucleon [24]. The analysis of experimental data is rather involved but over the years it has led to a reasonable consensus.
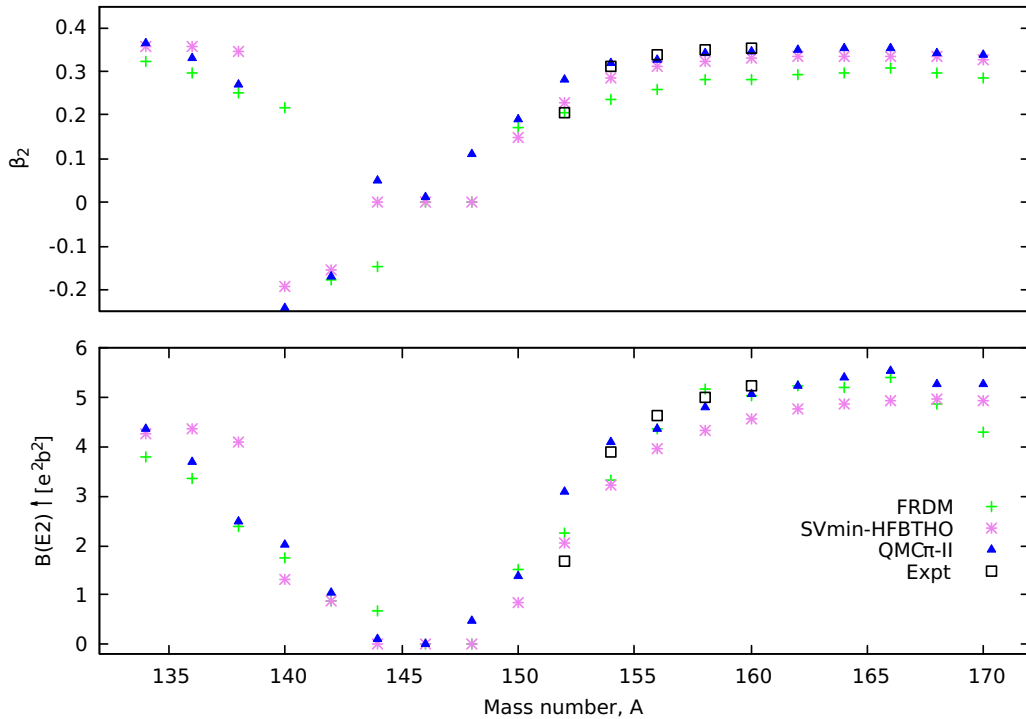


FIG. 12. Deformation parameter $\beta_2$ and corresponding transition probability $B(E2)\uparrow$ of Gd isotopes plotted against mass number, $A$. Values for FRDM are taken from Ref. [33], SV-min values are from Ref. [39], and the experimental data are from Ref. [47]. $B(E2)\uparrow$ are computed as in Ref. [47], using the respective $\beta_2$ values of the models. Plot legend is placed in the bottom panel.

Background-subtracted excitation spectra from inelastic scattering are subject to multidecomposition analysis, yielding multipole strength distribution as a function of excitation energy, $S(E)$, for each multipole. The moments of the strength function (the sum rules) are calculated as

$$m_k = \int dE \, E^k S(E). \qquad (27)$$

The centroid of the strength function $\tilde{E} = \frac{m_1}{m_0}$ but also other mean energies $\tilde{E}_k$ can be calculated from moment ratios,

$$\tilde{E}_k = \sqrt{\frac{m_k}{m_{k-2}}}. \qquad (28)$$

If the strength function is distributed in a narrow energy region, the mean energies $\tilde{E}_k$ are close together and can be interpreted as the energy of a resonance state.

The calculation has been performed using time-dependent Hartree-Fock (TDHF) technique [48]. The SKYAX code, modified by Newton [49] for calculation of giant resonances using Skyrme forces, has been further adapted for use with the QMC$\pi$-II model. To calculate giant resonance states, the TDHF equations have to be solved. This is achieved by using wave functions, obtained by solution of the static Hartree-Fock equations and evolve them in time following an external perturbation. The external perturbation consists of a spatial part $F(r)$, determining the type of resonance to be excited and the time profile $f(t)$ of the perturbation. For the isoscalar monopole resonance $F(r) = \sum_{i=1}^{A} r_i^2$ with $i$ being the label of a $i$th nucleon with a coordinate $r$ and

TABLE V. GMR energies (in MeV) of $^{208}$Pb, $^{144}$Sm, $^{116}$Sn, and $^{90}$Zr calculated from the QMC$\pi$-II and SV-min models. Errors from calculation are indicated in parentheses.

|            | QMC$\pi$-II  | SV-min       |
|------------|--------------|--------------|
| $^{208}$Pb | 13.79 (0.01) | 13.22 (0.07) |
| $^{144}$Sm | 15.29 (0.07) | 15.42 (0.15) |
| $^{116}$Sn | 16.02 (0.04) | 16.02 (0.20) |
| $^{90}$Zr  | 17.35 (0.15) | 17.47 (0.11) |

$f(t)$ has been taken to have a Gaussian shape. The strength function $S(E)$ is extracted from the TDHF calculation as the Fourier transform of the fluctuation of the expectation of $F(r)$, inducing the excitation, divided by the Fourier transform of the time profile $f(t)$ of the external perturbation. The GMR energy is then calculated as the centroid of $S(E)$, $\tilde{E}_0$. Details of the calculation will be presented elsewhere [50].

A recent collection of experimental data has been presented by Garg and Colò [24] in their Table I which includes GMR energies calculated as $\tilde{E}_3 = \sqrt{\frac{m_3}{m_1}}$, $\tilde{E}_1 = \sqrt{\frac{m_1}{m_{-1}}}$, $\tilde{E}_0 = \frac{m_1}{m_0}$ and has been used in this work to compare with the QMC$\pi$-II and SVmin results.

We show in Table V the numerical results of the calculation for $^{208}$Pb, $^{144}$Sm, $^{116}$Sn, and $^{90}$Zr for both the QMC$\pi$-II and SV-min models and a comparison with experimental data in Fig. 13. We find a very satisfactory agreement with experiment, confirming the value 230 MeV of incompressibility of
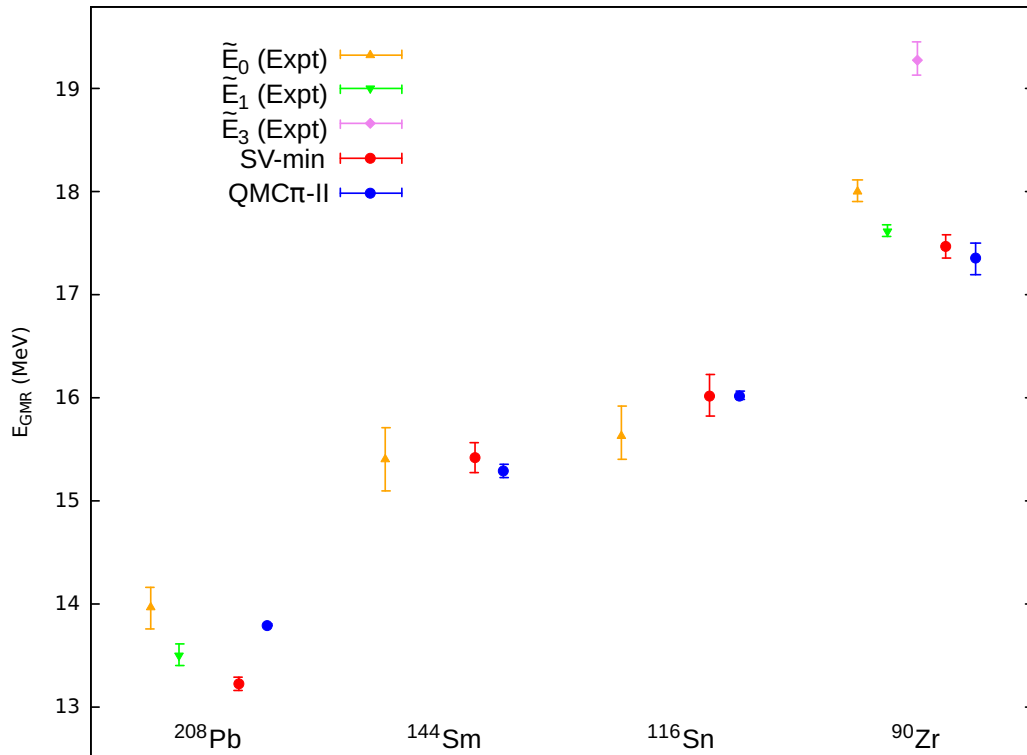


FIG. 13. GMR energies for $^{208}$Pb, $^{144}$Sm, $^{116}$Sn, and $^{90}$Zr from experiment and for the QMC$\pi$-II and SVmin models. Experimental data are taken from Table 1 of Ref. [24].
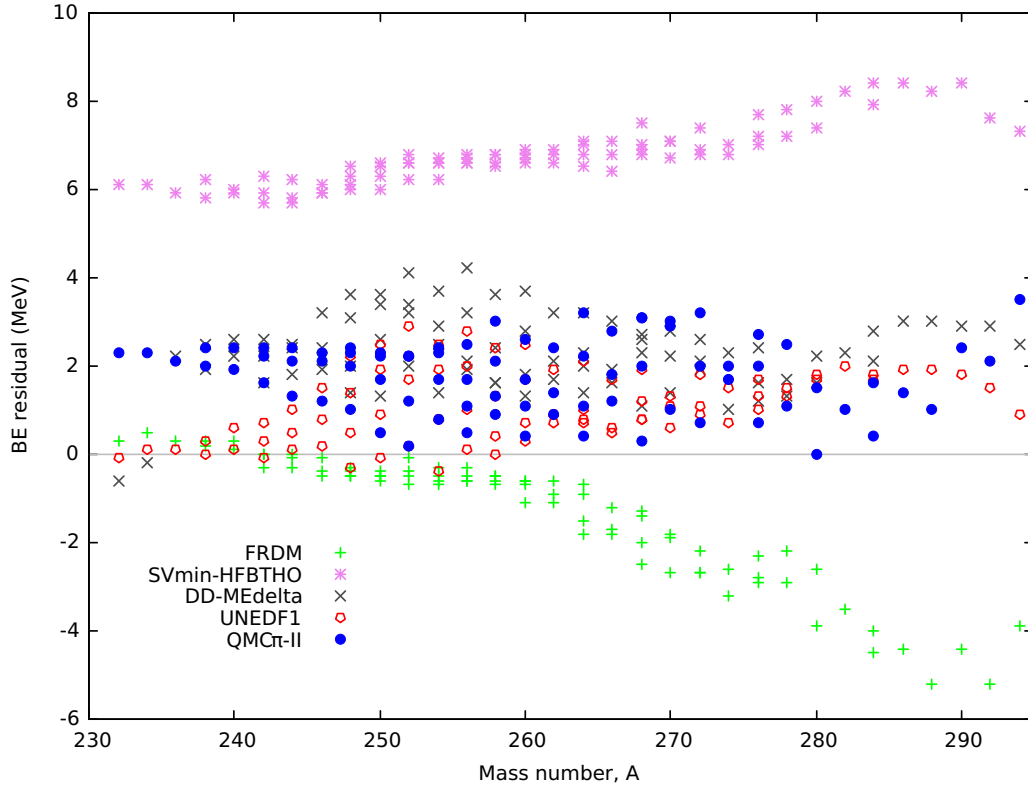
FIG. 14. SHE binding energy residuals for nuclei with $Z > 96$ plotted against mass number $A$. Also added for comparison are FRDM taken from Ref. [33], SV-min [13], UNEDF1 [30], and DD-ME$\delta$ [35], all taken from Ref. [39]. Experimental data used to compute the residuals are from Ref. [25].

the symmetric nuclear matter predicted in the present version of the QMC model.

### E. Binding energies of even-even superheavy nuclei

Calculations have also been extended to the superheavy elements with $Z \geqslant 96$, which were not included in the fit. Figure 14 shows the QMC predictions for binding energies in comparison with other models. The RMSD for binding energies for these nuclei, calculated with QMC$\pi$-II, is 2.0 MeV where FRDM and DD-ME$\delta$ give 1.9 and 2.5 MeV, respectively. The Skyrme force SV-min and UNEDF1 give 6.8 MeV and 1.4, respectively. The success of the QMC model in this region was also investigated in the QMC$\pi$-I where $\alpha$ decay energy and deformations were computed [10]. Further, using the previous version, detailed studies of superheavies including shell gaps and shape transition were carried out and reported in Ref. [51]. Predictions for these observables in SHE will certainly be done with the current QMC version as we move forward.

### V. CONCLUDING REMARKS

Parameter optimization of the new version of the quark-meson coupling model, QMC$\pi$-II, was carried out using the derivative-free algorithm POUNDerS. Parameter errors

and correlations were presented and the final parameter set was used to calculate various nuclear observables. QMC$\pi$-II produced nuclear matter properties within the acceptable range and showed considerable improvement for the slope of the symmetry energy, as well as for the incompressibility, compared to the values obtained in the previous QMC version. The new QMC parameters were also used to calculate ground state properties of even-even nuclei across the nuclear chart. The results were comparable to those of other well known models in the predictions for binding energies, rms charge radii, and pairing gaps. Calculations were extended to other nuclear observables which had not been part of the fit, including isotopic and isotonic shifts in energies and radii, skin thickness, and single-particle energies, for a number of chosen nuclei. Once again the results were found to be within a similar range to that produced by other models. Deformations were also investigated for gadolinium isotopes and are in agreement with available data. Isoscalar GMR calculations are particularly encouraging in the new QMC version, as it agrees very reasonably with various experimental results. Furthermore, the model appears to be effective in the superheavy region giving an rms binding energy residual of only 2.0 MeV. Calculations in this region and for unknown SHE up to the drip lines are currently in progress.

In the future, energy calculations will be further investigated for symmetric nuclei as well as in the region of the

$N = 50$ and $N = 82$ shell closures, where the current QMC residuals are relatively high compared to other regions in the nuclear chart. Charge radii, especially in the region of the mercury and platinum isotopes, and deformation properties of finite nuclei will be analyzed further. Odd-mass nuclei will also be studied using the QMC model. In addition, it will be interesting to explore the predictions for nuclei far from stability and currently unknown nuclei up to the proton and neutron drip lines.

[1] P. A. M. Guichon, Phys. Lett. B **200**, 235 (1988).

[2] P. A. M. Guichon, K. Saito, E. N. Rodionov, and A. W. Thomas, Nucl. Phys. A **601**, 349 (1996).

[3] P. A. M. Guichon and A. W. Thomas, Phys. Rev. Lett. **93**, 132502 (2004).

[4] P. A. M. Guichon, H. H. Matevosyan, N. Sandulescu, and A. W. Thomas, Nucl. Phys. A **772**, 1 (2006).

[5] K. Saito, K. Tsushima, and A. W. Thomas, Prog. Part. Nucl. Phys. **58**, 1 (2007).

[6] K. Tsushima, D.-H. Lu, A. W. Thomas, and K. Saito, Phys. Lett. B **443**, 26 (1998).

[7] S. D. Bass and A. W. Thomas, Phys. Lett. B **634**, 368 (2006).

[8] P. A. M. Guichon, A. W. Thomas, and K. Tsushima, Nucl. Phys. A **814**, 66 (2008).

[9] J. R. Stone, P. A. M. Guichon, P. G. Reinhard, and A. W. Thomas, Phys. Rev. Lett. **116**, 092501 (2016).

[10] J. Stone, P. Guichon, and A. Thomas, EPJ Web Conf. **163**, 00057 (2017).

[11] P. A. M. Guichon, J. R. Stone, and A. W. Thomas, Prog. Part. Nucl. Phys. **100**, 262 (2018).

[12] J. R. Stone and P. G. Reinhard, Prog. Part. Nucl. Phys. **58**, 587 (2007).

[13] P. Klüpfel, P.-G. Reinhard, T. J. Bürvenich, and J. A. Maruhn, Phys. Rev. C **79**, 034310 (2009).

[14] P. G. Reinhard (private communication).

[15] M. Kortelainen, T. Lesinski, J. Moré, W. Nazarewicz, J. Sarich, N. Schunck, M. V. Stoitsov, and S. Wild, Phys. Rev. C **82**, 024313 (2010).

[16] K. A. Olive *et al.* (Particle Data Group), Chin. Phys. C **38**, 090001 (2014).

[17] M. Bender, P.-H. Heenen, and P.-G. Reinhard, Rev. Mod. Phys. **75**, 121 (2003).

[18] M. Bender, K. Rutz, P. G. Reinhard, and J. A. Maruhn, Eur. Phys. J. A **8**, 59 (2000).

[19] K. W. Schmid and F. Grummer, Rep. Prog. Phys. **50**, 731 (1987).

[20] B.-A. Li and X. Han, Phys. Lett. B **727**, 276 (2013).

[21] J. R. Stone, N. J. Stone, and S. A. Moszkowski, Phys. Rev. C **89**, 044316 (2014).

[22] M. Dutra, O. Lourenco, J. S. Sa Martins, A. Delfino, J. R. Stone, and P. D. Stevenson, Phys. Rev. C **85**, 035201 (2012).

[23] D. H. Youngblood, H. L. Clark, and Y. W. Lui, Phys. Rev. Lett. **82**, 691 (1999).

[24] U. Garg and G. Colò, Prog. Part. Nucl. Phys. **101**, 55 (2018).

[25] M. Wang, G. Audi, F. Kondev, W. Huang, S. Naimi, and X. Xu, Chin. Phys. C **41**, 030003 (2017).

[26] I. Angeli and K. Marinova, At. Data Nucl. Data Tables **99**, 69 (2013).

[27] S. Balay, S. Abhyankar, M. F. Adams, J. Brown, P. Brune, K. Buschelman, L. Dalcin, V. Eijkhout, W. D. Gropp, D. Kaushik, M. G. Knepley, L. C. McInnes, K. Rupp, B. F. Smith, S. Zampini, H. Zhang, and H. Zhang, *PETSc Users Manual*, Tech. Rep. ANL-95/11 - Revision 3.7 (Argonne National Laboratory, Lemont, Illinois, 2016).

[28] S. Balay, W. D. Gropp, L. C. McInnes, and B. F. Smith, in *Modern Software Tools in Scientific Computing*, edited by E. Arge, A. M. Bruaset, and H. P. Langtangen (Birkhäuser Press, Boston, MA, 1997), pp. 163–202.

[29] T. Munson, J. Sarich, S. Wild, S. Benson, and L. C. McInnes, *Toolkit for Advanced Optimization (TAO) Users Manual*, Technical Report No. ANL/MCS-TM-322 - Revision 3.5 (Argonne National Laboratory, Lemont, Illinois, 2014).

[30] M. Kortelainen, J. McDonnell, W. Nazarewicz, P.-G. Reinhard, J. Sarich, N. Schunck, M. V. Stoitsov, and S. M. Wild, Phys. Rev. C **85**, 024304 (2012).

[31] M. Kortelainen, J. McDonnell, W. Nazarewicz, E. Olsen, P.-G. Reinhard, J. Sarich, N. Schunck, S. M. Wild, D. Davesne, J. Erler, and A. Pastore, Phys. Rev. C **89**, 054314 (2014).

[32] S. M. Wild, J. Sarich, and N. Schunck, J. Phys. G: Nucl. Part. Phys. **42**, 034031 (2015).

[33] P. Möller, A. J. Sierk, T. Ichikawa, and H. Sagawa, At. Data Nucl. Data Tables **109-110**, 1 (2016).

[34] N. Wan, C. Xu, and Z. Ren, Phys. Rev. C **94**, 044322 (2016).

[35] A. V. Afanasjev and S. E. Agbemava, Phys. Rev. C **93**, 054310 (2016).

[36] C. Qi and R. Wyss, Phys. Scr. **91**, 013009 (2016).

[37] H. De Witte, A. N. Andreyev, N. Barré, M. Bender, T. E. Cocolios, S. Dean, D. Fedorov, V. N. Fedoseyev, L. M. Fraille, S. Franchoo, V. Hellemans, P. H. Heenen, K. Heyde, G. Huber, M. Huyse, H. Jeppesen, U. Köster, P. Kunz, S. R. Lesher, B. A. Marsh *et al.*, Phys. Rev. Lett. **98**, 112502 (2007).

[38] R. Neugart, Europhys. News **48**, 12 (2017).

[39] http://massexplorer.frib.msu.edu, Last accessed on 2018-08-12.

[40] R. F. Garcia Ruiz *et al.*, Nat. Phys. **12**, 594 (2016).

[41] A. J. Miller, K. Minamisono, A. Klose, D. Garand, C. Kujawa, J. D. Lantis, Y. Liu, B. Maaß, P. F. Mantica, W. Nazarewicz, W. Nörtershäuser, S. V. Pineda, P.-G. Reinhard, D. M. Rossi, F. Sommer, C. Sumithrarachchi, A. Teigelhöfer, and J. Watkins, Nat. Phys. **15**, 432 (2019).

[42] P.-G. Reinhard and W. Nazarewicz, Phys. Rev. C **95**, 064328 (2017).

[43] M. Warda, M. Centelles, X. Vinas, and X. Roca-Maza, Acta Phys. Pol. B **43**, 209 (2012).

[44] C. M. Tarbert *et al.*, Phys. Rev. Lett. **112**, 242502 (2014).

[45] A. Trzcińska, J. Jastrzębski, P. Lubiński, B. Kłos, F. J. Hartmann, T. von Egidy, and S. Wycech, in *Physics with Ultra Slow Antiproton Beams*, edited by Y. Yamazaki and M. Wada, AIP Conf. Proc. No. 793 (AIP, Melville, NY, 2005), p. 214.

[46] H. Grawe, K. Langanke, and G. Martnez-Pinedo, Rep. Prog. Phys. **70**, 1525 (2007).

[47] S. Raman, C. W. G. Nestor, Jr, and P. Tikkanen, At. Data Nucl. Data Tables **78**, 1 (2001).

[48] P. D. Stevenson, M. R. Strayer, J. Rikovska Stone, and W. G. Newton, Int. J. Mod. Phys. E **13**, 181 (2004).

[49] W. G. Newton, Masters thesis, University of Tennessee, 2002.

[50] W. G. Newton and J. R. Stone (unpublished).

[51] J. R. Stone, K. Morita, P. A. M. Guichon, and A. W. Thomas, arXiv:1901.06064 [Phys. Rev. C (to be published)].